Revealing Plasmonic Gap Modes in Particle-on-Film Systems Using Dark-Field Spectroscopy

Dang Yuan Lei,[†,*] Antonio I. Fernández-Domínguez,[†,*] Yannick Sonnefraud,[†] Kannatassen Appavoo,[‡] Richard F. Haglund, Jr.,[‡] John B. Pendry,[†] and Stefan A. Maier[†]

[†]The Blackett Laboratory, Department of Physics, Imperial College London, London SW7 2AZ, United Kingdom, and [‡]Department of Physics and Astronomy, Vanderbilt University, Nashville, Tennessee 37235, United States

ABSTRACT

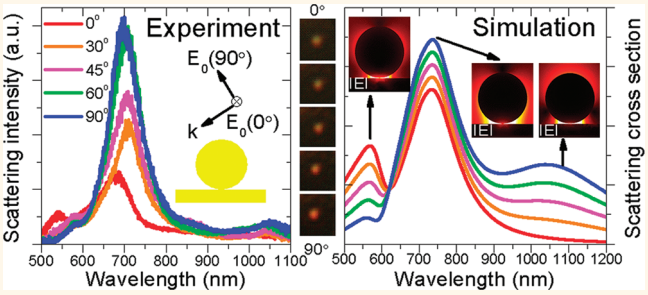

Polarization-controlled excitation of plasmonic modes in nanometric Au particle-on-film gaps is investigated experimentally using single-particle dark-field spectroscopy. Two distinct geometries are explored: nanospheres on top of and inserted in a thin gold film. Numerical simulations reveal that the three resonances arising in the scattering spectra measured for particles on top of a film originate from highly confined gap modes at the interface. These modes feature different azimuthal characteristics, which are consistent with recent theoretical transformation optics studies. On the other hand, the scattering maxima of embedded particles are linked to dipolar modes having different orientations and damping rates. Finally, the radiation properties of the particle–film gap modes are studied through the mapping of the scattered power within different solid angle ranges.

KEYWORDS: metal nanoparticles · particle–film interactions · plasmonic gap modes · single-particle spectroscopy · directional radiation

Surface plasmon excitations in metallic nanostructures are responsible for many fascinating optical phenomena such as surface-enhanced Raman scattering,[1] photoluminescence[2,3] and fluorescence[4,5] amplification, extraordinary transmission,[6,7] and superlensing effects.[8,9] Localized surface plasmon modes in either individual nanoparticles, particle dimers, or clusters are of particular interest because their optical properties can be readily designed and easily controlled over a wide spectral range. This can be achieved by tailoring particle shape and size[10] and the intra- and interparticle distances[11–17] on the nanoscale. Lately, it has been demonstrated that the exploitation of Fano resonances[18] in simple nanoparticle compounds makes the opening of a narrow frequency window possible, in which the interaction of these structures with radiation is strongly inhibited.[19,20] On the other hand, more recent theoretical studies have predicted that metal nanostructures with geometric singularities show a broad-band behavior, collecting and concentrating light efficiently over the whole visible regime.[21–24]

Localized plasmon resonances are highly sensitive to their surrounding environment, which makes them very suitable for biosensing purposes.[25] Thus, the nearby presence of a thin conducting film, for instance, modifies strongly the optical response of metal nanoparticles.[26] During the past decade, many theoretical[27–30] and experimental[31–36] works have been devoted to the analysis of plasmon coupling in particle–film geometries. These studies were inspired by the analogy between this problem and the strong interaction of fluorescent molecules with neighboring metal surfaces.[37] Two elegant theoretical tools have provided physical insights into the occurrence of plasmonic effects in these systems: plasmon hybridization[27] and transformation optics.[38] From the experimental side, surface-plasmon-assisted dipole–dipole interactions taking place between individual nanoparticles and metal surfaces have been thoroughly investigated,[31,32] and great efforts have been made to measure the effect of the particle–film separation on the spectral position of plasmon resonances.[35,39–41] However, there is very little knowledge about the transition of these plasmonic modes with the excitation

* Address correspondence to dangyuan.lei08@imperial.ac.uk, a.fernandez-dominguez@imperial.ac.uk.

Received for review October 31, 2011 and accepted January 18, 2012.

Published online January 18, 2012
10.1021/nn204190e

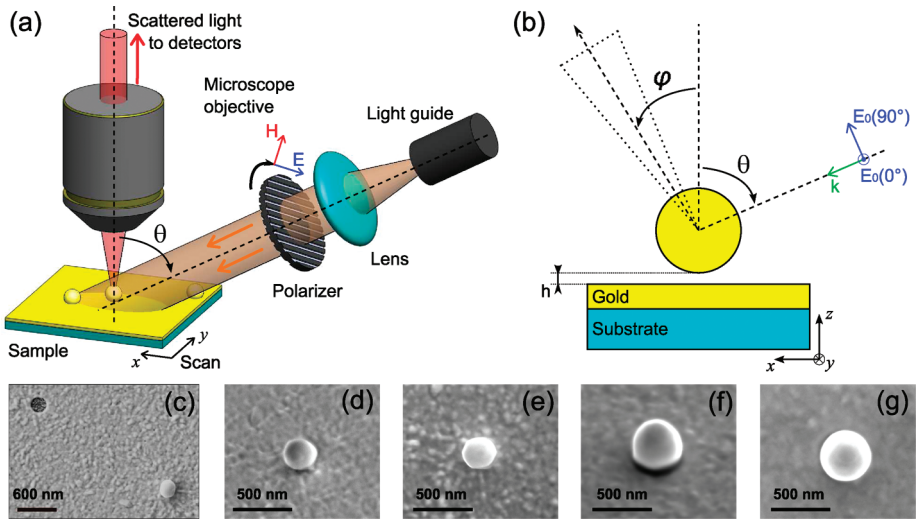

Figure 1. Schematics of the polarized side-illumination dark-field setup (a), and the simulation model (b) mimicking the experimental conditions. (c) SEM image of a dislodged Au nanoparticle and its corresponding hole. Oblique (d,f) and top (e,g) view SEM images for nanospheres of 230 nm (d,e) and 380 nm (f,g) diameter. Note the flat intersection region (shadow area) in (f).

polarization[33] or their directional radiation properties.

The optical response of nanoparticles inserted into a metal film is qualitatively different from their gapped counterparts. Before contact, the system of sphere and surface has no geometric singularities. However, if the sphere touches or intersects the surface, singularities emerge and the spectrum of plasmonic excitations is continuous and broad-band rather than discrete.[13,24] Although this geometry has been theoretically studied in the context of surface-enhanced Raman scattering,[42−44] very few experimental realizations of such nanostructures have been made so far. Moreover, partly embedded nanoparticles also serve as a defect, coupling efficiently free space radiation to propagating surface plasmons.[45−48] Thus, such a geometry becomes an ideal scenario for the analysis of the direct interaction between localized plasmon resonances sustained by metal nanoparticles and the surface plasmon polaritons supported by metallic films.

In this article, we demonstrate polarization-controlled excitation of plasmonic modes in self-assembled individual Au nanospheres on top of and inserted into a thin gold film. Single-particle dark-field spectra obtained from the former geometry feature three different scattering peaks whose relative intensity is strongly dependent on the incident polarization. Full-wave numerical simulations reveal that these resonances originate from tightly confined gap modes having different azimuthal characteristics, which are consistent with recent transformation optics studies. Similar measurements on the latter structure show two scattering maxima, which are linked to dipolar plasmonic modes having distinct orientations with respect to the film surface. Finally, in order to gain further physical insights into these plasmonic gap modes, their radiation properties are also investigated experimentally.

RESULTS AND DISCUSSION

The scattering measurements were carried out for individual Au nanospheres using dark-field spectroscopy with a polarization-adjustable white-light illumination at an incident angle $\theta = 70°$ with respect to the normal to the sample surface (see Figure 1a). Full-wave electromagnetic simulations based on the finite element method were performed for the experimental sample geometries and at conditions similar to the measurements. Figure 1b shows the simulation model used to isolate the fields scattered by the nanoparticle. This allows the integration of the power reirradiated by the nanospheres at different direction angles, φ, within a solid angle range defined by the numerical aperture of the microscope objective. The experimental Au particles were grown *via* self-assembly on the substrate film by depositing a thin layer (45 nm) of Au on top of a rough seed layer of 45 nm vanadium dioxide. The nanoparticles are either partially embedded into or standing on top of the film, as shown by the scanning electron microscopy (SEM) images in Figure 1c−g. Note that standing particles were always found in the vicinity of a hole in the film, as illustrated in panel c. This indicates that they were originated by the dislodgement of embedded nanoparticles, like the one displayed in panel f. The mechanisms leading to the formation of the extremely smooth nanospheres studied here are still under investigation, but they are likely to be related to the film agglomeration caused by the surface tension[49,50] between the seed and gold layers.

Figure 2a renders the scattering spectra measured from a standing nanosphere under different polarizations,

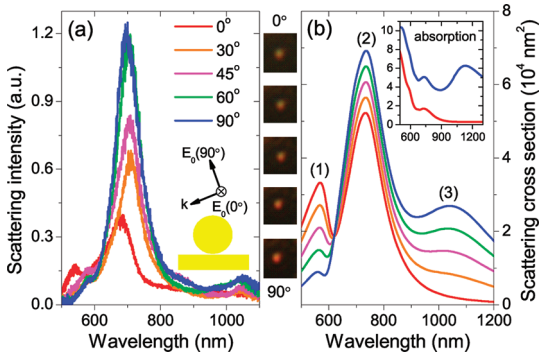

Figure 2. (a) Measured scattering spectra for a 155 nm diameter Au sphere standing on top of the Au film. (b) Simulated scattering cross sections for a 200 nm diameter Au sphere placed 2 nm above the Au film. Spectra in both panels and true-color dark-field images in the middle were obtained under different incident polarizations. The inset of panel b plots the absorption cross section of the same structure for 0 and 90° polarizations.

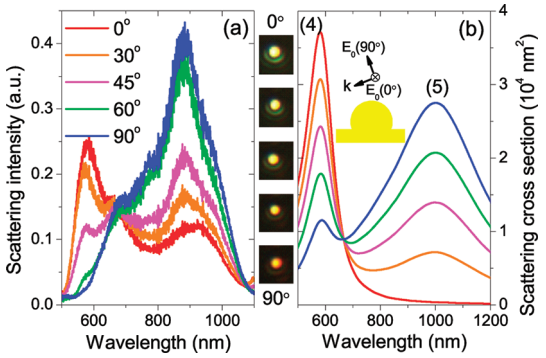

Figure 3. Measured (a) and simulated (b) scattering spectra and dark-field images (in the middle) for a Au sphere (218 nm diameter in experiment and 200 nm in simulation) partly embedded into the Au film. In both panels, spectra obtained under different incident polarizations are shown.

along with true-color dark-field images taken from the structure at different incident polarizations. As seen from the figure, a 155 nm diameter standing particle presents three scattering maxima within the frequency range under study. The height of the most intense (central) peak decreases when the incident plane wave is varied from p-polarization (90°, electric field in the plane of incidence) to s-polarization (0°, electric field parallel to the film surface). Note that the scattering amplitude of the two side peaks is also strongly dependent on the incoming polarization: the lower (larger) wavelength scattering maximum is more efficiently excited by s (p)-polarized light. These features are well reproduced by the numerical calculations displayed in Figure 2b. In accordance with the experimental values, the nanosphere diameter and film thickness in the simulations are set to 200 and 50 nm, respectively. The particle–film separation was adjusted to optimize the comparison with measured spectra. An excellent agreement between simulations and experiments is obtained for 2 nm separation (50 nm penetration) in the standing (embedded) configuration. The need for the inclusion of a small separation in the model for the standing geometry seems to indicate the presence of a nanoparticle–film gap in the experimental sample. The formation of this gap can be linked to the roughness of the Au film (see Figure 1), which prevents full contact between particle and substrate. Note that the discrepancy between the simulated and measured scattering intensities for the two side peaks can be linked to the different size of the theoretical (200 nm diameter) and experimental (155 nm diameter) nanoparticles.

Figure 3 presents the measured (a) and simulated (b) scattering spectra for the second geometry: a 218 nm diameter sphere partly embedded into the Au film. Both panels show the spectral transition from a broad long wavelength to a narrow short wavelength resonance as the incident polarization is varied from 90 to 0°. The different line width featured by these two resonances is linked to their distinct dipole moment strength and, hence, radiation damping rate. The dipolar character of these two resonances is discussed in detail below. Under 0° excitation (s-polarization), the dipole moment induced in the nanosphere is oriented parallel to the film surface. Charge transfer effects in such configuration are strongly inhibited, and the particle–film interaction is expected to be weak. This explains the narrow line width of this scattering peak, which resembles the sharp character of dipole resonances in isolated nanoparticles. On the other hand, 90° illumination (p-polarization) gives rise to a dipole moment normal to the film surface in the nanosphere. The formation of this resonance involves not only induced charges at the nanoparticle but also the sea of conduction electrons at the film substrate. This fact leads to a larger dipole strength and faster radiation damping rate. This explains why the long wavelength maxima in Figure 3 are broader than their short wavelength counterparts. Note that, contrary to simulation results, the experimental long wavelength resonance is not completely suppressed under s-polarization. This can be attributed to the presence of asymmetries and defects at the particle–film intersection in the experimental sample. These also explain the spectral broadening of the measured resonances with respect to the simulated ones, as the theoretical model does not account for such geometric imperfections.

In order to further understand the plasmonic modes responsible for the scattering peaks observed in the experimental and simulated spectra, the electric field distribution for the different particle–film resonances extracted from simulations is displayed in Figure 4. The modes are labeled following the notation in Figure 2b and Figure 3b. The first three columns display the electric field amplitude, $|E|$ (top panels), and its z-component, E_z (bottom panels), for the 2 nm gap geometry. The amplitude plots show that the electric field is strongly localized at the gap of the structure for these three resonances. Note that $|E|$ for peak 1 (3)

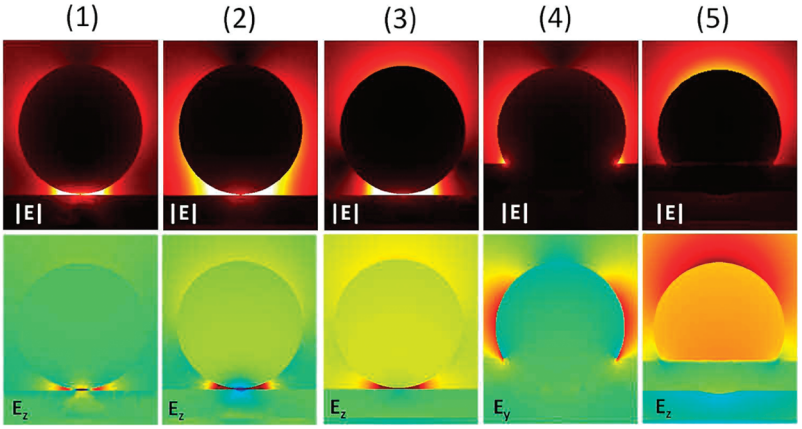

Figure 4. Total amplitude and dominant component of the electric field for the two systems under study. The electric field plots are evaluated at the different resonances labeled in Figure 2b and Figure 3b. In the upper panels, bright (dark) areas correspond to maximum (minimum) amplitude. In the lower panels, colors code the field component from negative (blue) to positive (red) maximum values. Both color scales are linear.

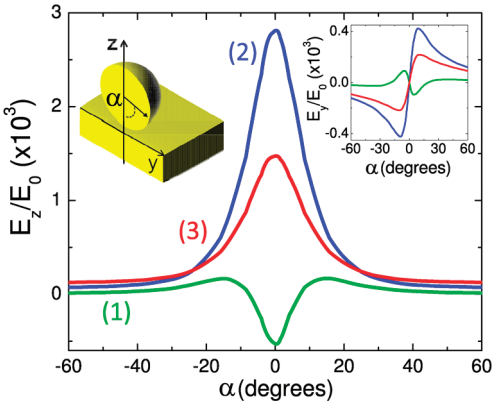

Figure 5. *z*-Component of the electric field evaluated along the nanosphere surface for the three scattering resonances sustained by the gapped geometry. The angle α is defined as shown in the left inset. The right inset plots the *y*-component of the electric field for the same conditions as the main panel.

presents two lateral (vertical) lobes, which indicate the parallel (normal) orientation of the dipolar plasmonic mode excited in the nanoparticle at the short (long) wavelength resonance. The field distribution for the central peak (2) spreads over the lateral dimension, which evidences the horizontal orientation of the nanoparticle dipole moment in this case. However, the lateral lobes for peak 2 extend into the gap, showing the hybrid nature of the underlying plasmonic mode. The complex field pattern featured by this mode enables it to couple efficiently to any incoming polarization, which explains the presence of the associated peak in all of the spectra shown in Figure 2.

The E_z panels for modes 1−3 in Figure 4 show that each resonance presents a well-defined number of field maxima at the particle−film gap. This is clearly observed in Figure 5, which displays linear plots of the *z*-component of the electric field as a function of α (see inset for definition) along the nanosphere surface. Whereas modes 2 and 3 exhibit a single field maximum at the gap, two maxima develop for the shorter wavelength mode. Moreover, note that the phase of E_z at α = 0° for mode 1 is the opposite of the other two modes. These observations, together with the antisymmetric profile of the parallel electric field shown in the inset of Figure 5, are in excellent agreement with previous theoretical predictions on a nanowire−plate geometry based on transformation optics.[38] This work demonstrates that each gap mode has a different azimuthal angular momentum, characterized by the number *n* of spatial periods covered by the electric fields along the surface of the two-dimensional particle. Transferring this picture to our three-dimensional structure, we can conclude that modes 2 and 3 in Figure 4 originate from gap modes with *n* = 1, whereas mode 1 is linked to an *n* = 2 angular momentum.

Figure 2b and panels 1−3 of Figure 4 indicate that care must be taken when relating the intensity of scattering maxima with the excitation efficiency of plasmonic resonances in the gapped structure. Note that although the scattering spectra seem to indicate that mode 2 is more efficiently excited than modes 1 and 3 under p-polarization, the absorption cross sections plotted in the inset of Figure 2b prove the contrary. This apparent contradiction results from the strong interaction between the nanoparticle localized plasmon mode and the propagating surface plasmon polaritons supported by the Au film at these two resonances. The lower panels in Figure 4 demonstrate that the resonating particle at modes 1 and 3 yields strong E_z gap fields. These intense normal electric fields allow the nanosphere to couple efficiently the incoming light to surface plasmon polaritons confined at the Au film.[45,47,48] These propagate away from the particle within the substrate plane, decaying due to absorption effects and experiencing very little radiation damping. This clarifies why these two plasmon modes give rise to strong absorption but weak scattering maxima for 90°

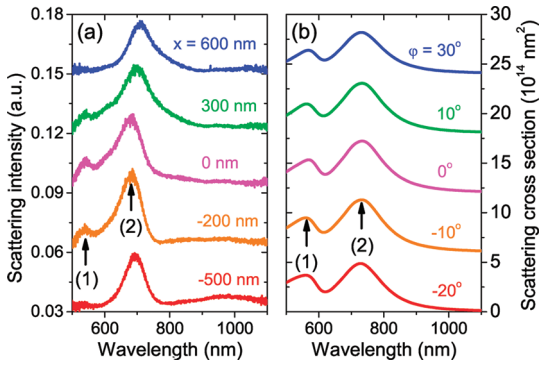

Figure 6. (a) Measured scattering spectrum for the 155 nm diameter sphere on top of the Au film when the collection position is varied along *x*-axis (see the definition in Figure 1a). (b) Simulated scattering cross sections as a function of the collection angle, φ (see the definition in Figure 1b), for the 200 nm diameter on top of the Au film. Both panels show results for 0° illumination. To highlight the spectral evolution, an offset was added to the data in both panels.

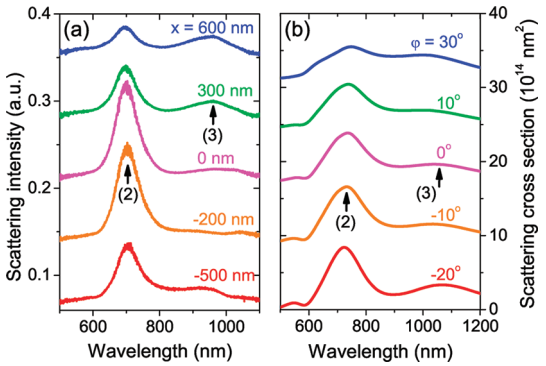

Figure 7. (a) Same measurements and simulations as Figure 6 were performed for the same structures under 90° illumination.

polarization. The spectra in the inset of Figure 2b also support our description of modes 1 and 2 (3) as being related to a strong dipole moment oriented parallel (normal) to the substrate surface. Note that, for 0° polarization, the former suffer strong absorption damping, whereas the latter is rather insensitive to it.

The last two columns in Figure 4 depict the electric field distribution for the partly embedded nanosphere. Both top and bottom panels show that strong dipole moments with distinct orientations are induced in the structure at resonance. In agreement with our previous discussion, these panels demonstrate that mode 4 (5) yields a strong lateral (vertical) induced dipole moment at the nanoparticle. Note that whereas mode 4, which is efficiently excited under s-polarization, leads to intense E_y fields, mode 5, which couples only to p-polarized light, exhibits a strong E_z component. This offers a means to the flexible tuning of field localization in this nanoparticle geometry through polarization.

Up to here, we have focused our attention on analyzing the near-field features of the plasmonic modes governing the scattering behavior of the two nanostructures under study. In the following, we investigate their radiation properties through the directional probing of the scattered fields. In the experiment, this is achieved by displacing the microscope objective along the sample (within the plane of incidence), as shown in Figure 1a. In the simulations, this is equivalent to rotating the plane of integration for the scattered Poynting vector, as illustrated in Figure 1b. Figure 6a plots the measured scattering spectra at different positions along the *x*-direction when the nanoparticle is illuminated with s-polarized light. Note that mode 1 is only detectable when the optical axis of the microscope objective is placed very close to the particle center (0 nm). This differs from the simulated spectra plotted in Figure 6b, where the scattering cross section shows little dependence on the collection angle φ. This difference is due to the small size of the Airy disk[35] of scattered light at short wavelengths, which leads to a significant reduction in the measured scattered signal when the microscope is displaced from the particle position. In contrast, mode 2 yields similar intensity peaks for all positions, which is in a good agreement with calculations in Figure 6b. The insensitivity of the scattered power measured from mode 2 to variations in the detector position originates from the strong dipole moment induced in the particle along *y*-direction (normal to the plane of incidence) for this resonance. The far-field radiation pattern for such an electric dipole moment features a doughnut-like radiation pattern around the *y*-direction, yielding equal radiation power along the positive and negative *x*-axis.

A richer physics is revealed by the evolution of the scattering spectra under p-polarized light. Figure 7 renders the measured and simulated scattering spectra for this case. The intensity of peak 2 decreases when the microscope objective optical axis is displaced away from the particle center in the experiment and when the integration plane is rotated to large φ in the simulation. This demonstrates that the scattered radiation for this plasmonic mode concentrates along the vertical direction. On the other hand, peak 3 features the opposite dependence on the detection position, showing an increase of the scattered signal for further measurements and calculations. This trend has been already observed in similar geometries[35,41] and can be interpreted as a consequence of the vertical dipolar character of the underlying plasmonic mode. The radiation profile emerging from such a dipole moment presents a toroid-like shape around the *z*-axis. This results in a weak radiation power along the vertical direction which, in turn, increases as the collection direction deviates from the vertical.

CONCLUSION

To conclude, complex plasmonic modes in individual nanospheres interacting with a metal film have

been investigated by single-particle dark-field spectroscopy and numerical simulations reproducing the experimental conditions. The origin of the scattering peaks found in measurements and calculations has been revealed by the electric field distributions calculated at resonance. The gapped particle−film geometry supports several gap modes, which can be associated with a well-defined azimuthal angular momentum. Two localized plasmonic modes have been reported when the nanosphere partly inserted into the substrate. Their origin resides in the formation of strong dipole moments either perpendicular or parallel to the film surface. Finally, the radiation properties of the gap modes supported by the former geometry have been studied both experimentally and theoretically, showing that the radiation pattern emerging from the nanosphere is strongly dependent on the incident polarization.

METHODS

The sample was fabricated on an ITO-covered glass substrate by means of (i) pulsed-laser ablation of a vanadium metal target (PLD: λ = 248 nm, 25 ns pulse duration, 3.84 J/cm^2 fluence, 10 Hz repetition rate, and 10 mTorr of O_2 gas) to render an amorphous, substoichiometric vanadium dioxide (45 nm $VO_{x=1.7}$ nominal thickness); (ii) thermal annealing (450 °C, O_2 gas at 250 mTorr for 40 min) to render the VO_2 film crystalline and stoichiometric; (iii) electron-beam evaporation of gold pellets at a rate of 0.5 Å/s, providing a Au film of 45 nm nominal thickness, as monitored by a quartz crystal microbalance. Focused ion-beam milling technique was used to mark the nanoparticles for subsequent spectroscopic measurements.

In the dark-field microscopy setup, the sample was illuminated by a polarized white light from a halogen bulb. A 50×, NA 0.55, IR-corrected microscope objective was used to collect the scattered light. For our numerical calculations, we used COMSOL Multiphysics, a commercial code implementing the finite element method in the frequency domain. In order to study the scattering properties of the gold nanospheres, we model the illumination as the incident plane wave plus the Fresnel waves reflected by the bare substrate. This way, the field components scattered by the nanoparticle itself were isolated from the contribution coming from the gold film.[51]

Conflict of Interest: The authors declare no competing financial interest.

Acknowledgment. The authors acknowledge support by the UK Engineering and Physical Sciences Research Council (EPSRC). D.Y.L. and Y.S. acknowledge funding from the Leverhulme Trust. A.I.F.-D. acknowledges funding from the EU IEF Marie Curie program and ESF Plasmon-Nanobiosense network. K.A. and R.F.H. acknowledge funding from the National Science Foundation (NSF) (ECE-0801980) and DTRA (HDTRA1-10-1-0016). Portions of this work were performed at the Vanderbilt Institute of Nanoscale Science and Engineering, using facilities renovated under NSF ARI-R2 DMR-0963361.

REFERENCES AND NOTES

1. Kneipp, K.; Kneipp, H.; Itzkan, I.; Dasari, R. R.; Feld, M. Ultrasensitive Chemical Analysis by Raman Spectroscopy. *Chem. Rev.* **1999**, *99*, 2957–2975.
2. Okamoto, K.; Niki, I.; Shvartser, A.; Narukawa, Y.; Mukai, T.; Scherer, A. Surface-Plasmon-Enhanced Light Emitters Based on InGaN Quantum Wells. *Nat. Mater.* **2004**, *3*, 601–605.
3. Lei, D. Y.; Li, J.; Ong, H. C. Tunable Surface Plasmon Mediated Emission from Semiconductors by Using Metal Alloys. *Appl. Phys. Lett.* **2007**, *91*, 021112.
4. Geddes, C. D. *Metal-Enhanced Fluorescence*; John Wiley & Sons, Inc.: New York, 2010.
5. Giannini, V.; Fernández-Domínguez, A. I.; Heck, S. C.; Maier, S. A. Plasmonic Nanoantennas: Fundamentals and Their Use in Controlling the Radiative Properties of Nanoemitters. *Chem. Rev.* **2011**, *111*, 3888–3912.
6. Ebbesen, T. W.; Lezec, H. J.; Ghaemi, H. F.; Thio, T.; Wolff, P. A. Extraordinary Optical Transmission through Subwavelength Hole Arrays. *Nature* **1998**, *391*, 667–669.
7. García-Vidal, F. J.; Martín-Moreno, L.; Ebbesen, T. W.; Kuipers, K. Light Passing through Subwavelength Apertures. *Rev. Mod. Phys.* **2010**, *82*, 729–787.
8. Pendry, J. B. Negative Refraction Makes a Perfect Lens. *Phys. Rev. Lett.* **2000**, *85*, 3966–3969.
9. Fang, N; Lee, H.; Sun, C.; Zhang, X. Sub-Diffraction-Limited Optical Imaging with a Silver Superlens. *Science* **2005**, *308*, 534–537.
10. Bohren, C.; Huffman, D. *Absorption and Scattering of Light by Small Particles*; Wiley: New York, 1983.
11. Prodan, E.; Radloff, C.; Halas, N. J.; Nordlander, P. A Hybridization Model for the Plasmon Response of Complex Nanostructures. *Science* **2003**, *302*, 419–422.
12. Atay, T.; Song, J.-H.; Nurmikko, V. Strongly Interacting Plasmon Nanoparticle Pairs: From Dipole−Dipole Interaction to Conductively Coupled Regime. *Nano Lett.* **2004**, *4*, 1627–1631.
13. Aubry, A.; Lei, D. Y.; Maier, S. A.; Pendry, J. B. Interaction between Plasmonic Nanoparticles Revisited with Transformation Optics. *Phys. Rev. Lett.* **2010**, *105*, 233901.
14. Brown, L. V.; Sobhani, H.; Lassiter, J. B.; Nordlander, P.; Halas, N. J. Heterodimers: Plasmonic Properties of Mismatched Nanoparticle Pairs. *ACS Nano* **2010**, *4*, 819–832.
15. Banerjee, P.; Conklin, D.; Nanayakkara, S.; Park, T.-H.; Therien, M. J.; Bonnell, D. A. Plasmon-Induced Electrical Conduction in Molecular Devices. *ACS Nano* **2010**, *4*, 1019–1025.
16. Slaughter, L. S.; Wu, Y.; Willingham, B. A.; Nordlander, P.; Link, S. Effects of Symmetry Breaking and Conductive Contact on the Plasmon Coupling in Gold Nanorod Dimers. *ACS Nano* **2010**, *4*, 4657–4666.
17. Lei, D. Y.; Aubry, A.; Maier, S. A.; Pendry, J. B. Plasmonic Interaction between Overlapping Nanowires. *ACS Nano* **2010**, *5*, 597–607.
18. Lukyanchuk, B.; Zheludev, N. I.; Maier, S. A.; Halas, N. J.; Nordlander, P. A.; Giessen, H.; Chong, C. T. The Fano Resonance in Plasmonic Nanostructures and Metamaterials. *Nat. Mater.* **2010**, *9*, 707–715.
19. Verellen, N.; Sonnefraud, Y.; Sobhani, H.; Hao, F.; Moshchalkov, V. V.; Dorpe, P. V.; Nordlander, P.; Maier, S. A. Fano Resonances in Individual Coherent Plasmonic Nanocavities. *Nano Lett.* **2009**, *9*, 1663–1667.
20. Sonnefraud, Y.; Verellen, N.; Sobhani, H.; Vandenbosch, G. A.; Moshchalkov, V. V.; Dorpe, P. V.; Nordlander, P.; Maier, S. A. Experimental Realization of Subradiant, Superradiant, and Fano Resonances in Ring/Disk Plasmonic Nanocavities. *ACS Nano* **2010**, *4*, 1664–1670.
21. Aubry, A.; Lei, D. Y.; Fernández-Domínguez, A. I.; Sonnefraud, Y.; Maier, S. A.; Pendry, J. B. Plasmonic Light Harvesting Devices over the Whole Visible Spectrum. *Nano Lett.* **2010**, *10*, 2574–2579.
22. Aubry, A.; Lei, D. Y.; Maier, S. A.; Pendry, J. B. Broadband Plasmonic Device Concentrating the Energy at the Nanoscale: The Crescent-Shaped Cylinder. *Phys. Rev. B* **2010**, *82*, 125430.

23. Lei, D. Y.; Aubry, A.; Maier, S. A.; Pendry, J. B. Broadband Nano-Focusing of Light Using Kissing Nanowires. *New J. Phys.* **2010**, *12*, 093030.
24. Fernández-Domínguez, A. I.; Maier, S. A.; Pendry, J. B. Collection and Concentration of Light by Touching Spheres: A Transformation Optics Approach. *Phys. Rev. Lett.* **2010**, *105*, 266807.
25. Anker, J. N.; Hall, W. P.; Lyandres, O.; Shah, N. C.; Zhao, J.; Van Duyne, R. P. Biosensing with Plasmonic Nanosensors. *Nat. Mater.* **2008**, *7*, 442–453.
26. Holland, W. R.; Hall, D. G. Frequency Shift of an Electric-Dipole near a Conducting Surface. *Phys. Rev. Lett.* **1984**, *52*, 1041–1044.
27. Nordlander, P.; Prodan, E. Plasmon Hybridization in Nanoparticles near Metallic Surfaces. *Nano Lett.* **2004**, *4*, 2209–2213.
28. Papanikolaou, N. Optical Properties of Metallic Nanoparticle Arrays on a Thin Metallic Film. *Phys. Rev. B* **2007**, *75*, 235426.
29. Garíca de Abajo, F. J. Colloquium: Light Scattering by Particle and Hole Arrays. *Rev. Mod. Phys.* **2007**, *79*, 1267–1290and references therein.
30. Vernon, K. C.; Funston, A. M.; Novo, C.; Gómez, D. E.; Mulvaney, P.; Davis, T. J. Influence of Particle−Substrate Interaction on Localized Plasmon Resonances. *Nano Lett.* **2010**, *10*, 2080–2086.
31. Stuart, H. R.; Hall, D. G. Enhanced Dipole−Dipole Interaction between Elementary Radiators near a Surface. *Phys. Rev. Lett.* **1998**, *80*, 5663–5666.
32. Félidj, N.; Aubard, J.; Lévi, G.; Krenn, J. R.; Schider, G.; Leitner, A.; Aussenegg, F. R. Enhanced Substrate-Induced Coupling in Two-Dimensional Gold Nanoparticle Arrays. *Phys. Rev. B* **2002**, *66*, 245407.
33. Le, F.; Lwin, N. Z.; Steele, J. M.; Kll, M.; Halas, N. J.; Nordlander, P. Plasmons in the Metallic Nanoparticle−Film System as a Tunable Impurity Problem. *Nano Lett.* **2005**, *5*, 2009–2013.
34. He, L.; Smith, E. A.; Natan, M. J.; Keating, C. D. The Distance-Dependence of Colloidal Au-Amplified Surface Plasmon Resonance. *J. Phys. Chem. B* **2004**, *108*, 10973–10980.
35. Mock, J. J.; Hill, R. T.; Degiron, A.; Zauscher, S.; Chilkoti, A.; Smith, D. R. Distance-Dependent Plasmon Resonant Coupling between a Gold Nanoparticle and Gold Film. *Nano Lett.* **2008**, *8*, 2245–2252.
36. Yamamoto, N.; Ohtani, S.; Garíca de Abajo, F. J. Gap and Mie Plasmons in Individual Silver Nanospheres near a Silver Surface. *Nano Lett.* **2011**, *11*, 91–95.
37. Chance, R. R.; Prock, A.; Silbey, R. Molecular Fluorescence and Energy Transfer near Interfaces. *Adv. Chem. Phys.* **1978**, *37*, 1–65.
38. Aubry, A.; Lei, D. Y.; Maier, S. A.; Pendry, J. B. Plasmonic Hybridization between Nanowires and a Metallic Surface: A Transformation Optics Approach. *ACS Nano* **2011**, *5*, 3293–3308.
39. Hu, M.; Ghoshal, A.; Marquez, M.; Kik, P. G. Single Particle Spectroscopy Study of Metal-Film-Induced Tuning of Silver Nanoparticle Plasmon Resonances. *J. Phys. Chem. C* **2010**, *114*, 7509–7514.
40. Okamoto, T.; Yamaguchi, T. Optical Absorption Study of the Surface Plasmon Resonance in Gold Nanoparticles Immobilized onto a Gold Substrate by Self-Assembly Technique. *J. Phys. Chem. B* **2003**, *107*, 10321–10324.
41. Hill, R. T.; Mock, J. J.; Urzhumov, Y.; Sebba, D. S.; Oldenburg, S. J.; Chen, S. Y.; Lazarides, A. A.; Chilkoti, A.; Smith, D. R. Leveraging Nanoscale Plasmonic Modes To Achieve Reproducible Enhancement of Light. *Nano Lett.* **2010**, *10*, 4150–4154.
42. García-Vidal, F. J.; Pendry, J. B. Collective Theory for Surface Enhanced Raman Scattering. *Phys. Rev. Lett.* **1996**, *77*, 1163–1166.
43. Xu, H.; Aizpurua, J.; Käll, M.; Apell, P. Electromagnetic Contributions to Single-Molecule Sensitivity in Surface-Enhanced Raman Scattering. *Phys. Rev. E* **2000**, *62*, 4318–4324.
44. Luo, Y.; Aubry, A.; Pendry, J. B. Electromagnetic Contribution to Surface-Enhanced Raman Scattering from Rough Metal Surfaces: A Transformation Optics Approach. *Phys. Rev. B* **2011**, *83*, 155422.
45. Shchegrov, A. V.; Novikov, I. V.; Maradudin, A. A. Scattering of Surface Plasmon Polaritons by a Circularly Symmetric Surface Defect. *Phys. Rev. Lett.* **1997**, *78*, 4269–4272.
46. Sánchez-Gil, J. A.; Maradudin, A. A. Near-Field and Far-Field Scattering of Surface Plasmon Polaritons by One-Dimensional Surface Defects. *Phys. Rev. B* **1999**, *60*, 8359–8367.
47. Chang, S. H.; Gray, S. K.; Schatz, G. C. Surface Plasmon Generation and Light Transmission by Isolated Nanoholes and Arrays of Nanoholes in Thin Metal Films. *Opt. Express* **2005**, *13*, 3150–3165.
48. Nikitin, A. Y.; García-Vidal, F. J.; Martín-Moreno, L. Surface Electromagnetic Field Radiated by a Subwavelength Hole in a Metal Film. *Phys. Rev. Lett.* **2010**, *105*, 073902.
49. Pillai, S.; Catchpole, K. R.; Trupke, T.; Green, M. A. Surface Plasmon Enhanced Silicon Solar Cells. *J. Appl. Phys.* **2007**, *101*, 093105.
50. Beck, F. J.; Polman, A; Catchpole, K. R. Tunable Light Trapping for Solar Cells Using Localized Surface Plasmons. *J. Appl. Phys.* **2009**, *105*, 114310.
51. Knight, M. W.; Fan, J.; Capasso, F.; Halas, N. J. Influence of Excitation and Collection Geometry on the Dark Field Spectra of Individual Plasmonic Nanostructures. *Opt. Express* **2010**, *18*, 2579–2587.